Changes in End Effector Trajectory Jitter Amplitude under the Interaction of Lerobot Diffusion Policy Denoising Steps and SLAM Loopback Frequency

Mingyang Cui[1], Hutchinson Seth[2]
[1]Northeastern University, College of Engineering
[2]Khoury College of Computer Sciences, Department of Electrical and Computer Engineering, Northeastern University
Corresponding author: Mingyang Cui (e-mail: cui.mingya0824@gmail.com).

ABSTRACT This study investigates the interaction between the number of denoising steps in a LeRobot Diffusion Policy and the frequency of Simultaneous Localization and Mapping loop-closure corrections on end-effector trajectory jitter in mobile manipulation systems. A controlled experimental framework was established in which the robotic arm motion path and disturbance magnitude were held constant while denoising-step levels and loop-closure frequencies were independently varied. End-effector trajectories were collected in Cartesian space, and high-frequency jitter components were extracted to quantify trajectory instability. Two-way analysis of variance was employed to evaluate the main effects and interaction effect of the two factors. The results reveal a statistically significant interaction effect, indicating that the effectiveness of denoising-step adjustment depends strongly on loop-closure frequency. Under low-frequency disturbance conditions, increasing the number of denoising steps reduced the normalized jitter amplitude to approximately 47% of the baseline level. However, under high-frequency disturbance conditions, the same adjustment reduced the normalized jitter amplitude only to approximately 83% of the baseline level, demonstrating a substantial decline in suppression effectiveness. Frequency-domain analysis further shows that dense loop-closure disturbances can induce delayed compensation and low-frequency energy accumulation when excessive smoothing is applied, thereby limiting the benefits of additional denoising steps. These findings reveal a parameter dependency boundary between policy smoothing strength and disturbance frequency and provide a quantitative basis for coordinated configuration of perception and control modules, contributing to improved trajectory smoothness and operational stability in mobile manipulation robots operating in dynamic environments.

INDEX TERMS LeRobot Diffusion Policy; SLAM Loop Jump Frequency; End-Effector Trajectory Jitter; Interaction Effect; Denoising Steps

I. INTRODUCTION

THE precision operation capability of mobile manipulation robots in dynamic environments depends on the close coordination between the perception system and the motion control strategy. In systems based on the LeRobot Diffusion Policy framework, the number of denoising steps in the diffusion strategy directly affects the temporal smoothness of the generated action sequence, while the global correction of the base pose by the localization and mapping module at the moment of loop closure introduces a step disturbance [1]-[2]. Current research lacks quantitative explanation of the interaction between the number of denoising steps and the loop jump frequency on the amplitude of end effector trajectory jitter. Clarifying this relationship has direct engineering value for improving the operation accuracy and motion stability of mobile manipulation robots in unstructured environments, and also provides a theoretical constraint for the selection of diffusion strategy parameters under perceived disturbance conditions.

Quantitatively characterizing the interaction between the number of denoising steps and the loopback frequency on end-effector jitter requires addressing the analytical difficulties arising from the deep coupling between the sensing and control modules in the frequency domain [3]-[4]. The base pose jump caused by SLAM loopback correction is a deterministic step signal, the timing and frequency of which are determined by the distribution of environmental characteristics and are not regulated by the control strategy [5]-[6]. The denoising process of the Diffusion Policy endows the motion generation path with a low-pass filtering effect;

the higher the number of denoising steps, the narrower the system bandwidth and the greater the phase lag in response to external disturbances [7]-[8]. This cross-module characteristic constitutes an implicit frequency matching constraint: the relative relationship between the strategy bandwidth and the disturbance frequency determines the amplitude trend of end-effector jitter, but the two are not independent additive factors, and their coupling effect cannot be fully explained by analyzing either variable alone. The resulting dilemma is that the selection of the number of denoising steps lacks differentiated basis for different loopback frequency conditions.

To address the issues of motion smoothness and external disturbance suppression in diffusion strategies, existing research has explored solutions from two directions: strategy parameter optimization and perception robustness enhancement. On the strategy side, some works balance motion response speed and trajectory smoothness by adjusting the number of denoising steps, or introduce temporal consistency constraints to enhance the continuity of generated trajectories. However, these methods assume the base pose remains stable and do not consider the step impact of loop closure jumps on the observed input [9]-[10]. On the perception side, researchers have proposed loop closure detection delay triggering mechanisms or pose graph smoothing interpolation strategies to mitigate the impact of jumps. However, these methods, by modifying the SLAM backend behavior to suppress disturbances, may introduce positioning lag or accuracy loss [11]-[12]. In summary, existing approaches treat the selection of the number of denoising steps and the impact of loop closure jumps as independent problems, without addressing their interaction in the frequency domain. Therefore, whether there is a conditional dependence between the number of denoising steps and the SLAM loop closure jump frequency when they jointly affect the end-effector jitter amplitude, and the direction and strength of this dependence, remains to be systematically investigated.

To answer the aforementioned questions, this paper designs a two-variable controlled experimental framework to quantitatively analyze the interaction between the number of denoising steps in the LeRobot Diffusion Policy and the SLAM loop transition frequency on the amplitude of end effector trajectory jitter. The study fixes the robot arm's motion path and the base disturbance amplitude, independently adjusting the denoising step level and the simulated loop transition frequency level. The end effector's Cartesian space trajectory is collected, and high-frequency jitter components are extracted as observation indicators. A two-way analysis of variance (ANOVA) is used to test the statistical significance of the interaction effect. Experimental results show that the suppression effectiveness of the denoising step number on end effector jitter amplitude decreases sharply with increasing loop transition frequency. Under low-frequency disturbance conditions, increasing the denoising step number significantly suppresses jitter amplitude; under high-frequency disturbance conditions, the suppression amplitude contributed by the same increase in denoising step number is compressed, and the residual suppression ability is much weaker than in the low-frequency state, with the interaction effect reaching a statistically significant level. The research results define the parameter dependence boundary of the end-point trajectory smoothness constrained by the number of denoising steps and the loop transition frequency, providing a quantitative basis for cross-module collaborative configuration of mobile operation strategies under the LeRobot framework.

II. JITTER MEASUREMENT METHOD UNDER TWO INDEPENDENT VARIABLE INTERACTIONS

A. DEFINITION OF INDEPENDENT VARIABLES AND REGULATORY PATHWAYS

The mobile operation platform consists of an omnidirectional mobile chassis, a six-degree-of-freedom collaborative robotic arm, and an onboard computing unit. The LeRobot Diffusion Policy is deployed on the onboard computing unit and connected to the robotic arm joint controller [13]. The diffusion strategy generates an action sequence based on the observation sequence. The observation sequence includes the joint angle position of the robotic arm, the joint angular velocity, and the pose of the target object relative to the base coordinate system obtained by the SLAM module [14]-[15]. The denoising step count N is defined as the total number of steps from the initial noise distribution iteration to the action output during the backsampling process of the diffusion model. The SLAM loop jump frequency f refers to the number of times the base pose undergoes a step correction per unit time. In real-world scenarios, the pose map optimization at the moment of loop closure resets the odometry cumulative drift to a globally consistent estimate. This correction process is reflected as an instantaneous jump in the base pose [16]-[17]. To independently manipulate f under controlled conditions, this study uses a simulated injection method to generate a base step perturbation sequence with a predetermined time interval. The perturbation amplitude is fixed at a constant value A_{jump}, and the frequency level is divided into several levels based on the number of perturbations per unit time [18].

During system operation, the Diffusion Policy outputs the target pose command to the end effector, and the built-in servo controller of the robotic arm drives the joint to track the command [19]. The response characteristics of the Diffusion Policy to changes in observation are determined by the iteration depth of the denoising process [20]. Let the observation condition be o, the intermediate action state of the k-th denoising step be a_k, and the sampling recursion relationship of the diffusion model be:

$$a_{k-1} = \frac{1}{\sqrt{\alpha_k}}\left(a_k - \frac{1-\alpha_k}{\sqrt{1-\bar{\alpha}_k}}\epsilon_\theta(a_k, k, o)\right) + \sigma_k z \quad (1)$$

In the formula, α_k and $\bar{\alpha}_k$ are noise scheduling parameters;

ϵ_θ is the noise prediction network; σ_k is the sampling variance; $z \sim N(0, I)$ is standard Gaussian noise. The recursive process imparts a low-pass filtering effect to the motion generation path: increasing N reduces the dependence of the motion sequence on the high-frequency components in the observation, and the response to external abrupt changes tends to be smoother. When a SLAM loop jump causes a step change in o, the compensation command output by the Diffusion Policy is adjusted by N in both amplitude and phase. This adjustment is transmitted to the end effector via the servo controller, generating additional high-frequency oscillations in the end effector's motion trajectory. The SLAM loop-corrected injection observation path and the Diffusion Policy denoising and recursive generation of motion commands constitute a signal closed loop with the combined effect of N and f. Within this closed loop, the adjustment paths of N and f achieve dual decoupling of the physical link and computational timing: changes in f only affect the SLAM observation injection stage, and changes in N only affect the Diffusion Policy inference stage. Both the independent adjustment and joint effect of these two on the end-effector motion converge through the common channel of the robotic arm's end-effector motion. This decoupling design provides the structural premise for the independent manipulation and statistical separation of interaction effects.

B. SIMULATED SLAM LOOP-JUMPING FREQUENCY INJECTION METHOD

In the closed-loop architecture described above, the independent manipulation of f is achieved by injecting a base step perturbation with a fixed amplitude and adjustable time interval into the SLAM observation path. The timing and amplitude of the actual SLAM loop transition are determined by the environmental feature matching results, and cannot be preset or repeatedly manipulated in physical experiments [21]. If the loop transition frequency f is directly governed by environmental features, the experimental conditions corresponding to different frequency levels cannot be reproduced under controlled conditions, and the influence of frequency on the end jitter amplitude cannot be separated from the mixed environmental factors. The way to solve this dilemma is to construct a base pose perturbation sequence with a fixed amplitude and adjustable time interval, and replace the actual loop correction with a simulated injection method, so that the frequency f becomes an independent variable that can be manipulated independently in the experiment.

The perturbation injection point is selected in the observation path of the SLAM module outputting the target pose estimation to the Diffusion Policy [22]. The original base pose estimate output by the SLAM module at time t is denoted as the homogeneous transformation matrix $T_{\text{base}}^{\text{raw}}(t)$. The base pose estimate $T_{\text{base}}^{\text{pert}}(t)$ after perturbation is obtained by right-multiplying by the perturbation transformation matrix $T_{\text{jump}}(t)$. This injection method simulates the instantaneous correction applied to the base node by pose map optimization during loop closure: the original odometry estimate is forced to move towards a globally consistent pose at the loop closure time. This process is mathematically equivalent to right-multiplying by a correction transformation. The injection relationship is expressed as:

$$T_{\text{base}}^{\text{pert}}(t) = T_{\text{base}}^{\text{raw}}(t) \cdot T_{\text{jump}}(t) \tag{2}$$

The rotation component of the perturbation transformation matrix $T_{\text{jump}}(t)$ is set as an identity matrix to eliminate the additional contribution of rotational degrees of freedom to end jitter, and the translation component amplitude is fixed as a constant value A_{jump} to force the impact intensity of each jump to be equal. This matrix only undergoes a step change at discrete times, and maintains an identity transformation in other time periods, thus forming a piecewise constant perturbation sequence in the time domain.

The jump frequency f is controlled by adjusting the time interval Δt between two adjacent steps, and the two satisfy the reciprocal relationship $\Delta t = 1/f$. The total experimental duration T_{total} is divided into several time slots with an interval Δt. At the beginning of each time slot, a step disturbance is injected at $t_i = i \cdot \Delta t$. In order to simulate the randomness of the cyclic correction direction in the real environment, the disturbance direction is cyclically selected in the horizontal plane according to the preset angle set $\Theta = \{\theta_1, \theta_2, \ldots, \theta_m\}$ [23]. The translation vector δ_i of the i-th disturbance has a constant amplitude of A_{jump} and a direction angle of θ_i. Its component form is:

$$\delta_i = A_{\text{jump}} \cdot [\cos\theta_i, \sin\theta_i, 0]^\top \tag{3}$$

This construction method makes the disturbance sequence exhibit clear parameterization characteristics in the time domain: the amplitude is determined by A_{jump}; the time density is determined by f; the direction mode is determined by Θ. The difference in Δt values corresponding to different frequency levels directly determines the density of transition edges within the same time window. The higher the frequency, the smaller Δt, and the more step disturbances are injected per unit time. This rule is particularly evident between the three frequency gradients of 0.05Hz, 0.2Hz and 1.0Hz, as shown in Figure 1.

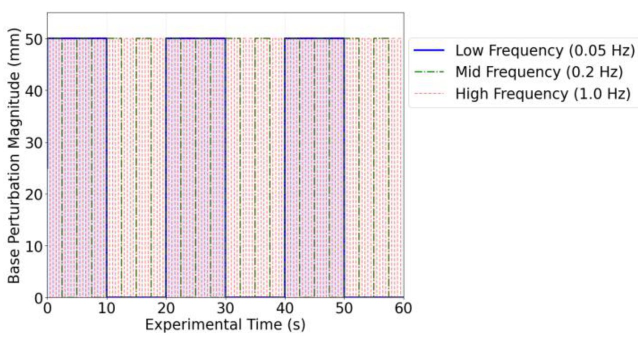

FIGURE 1. Timing signal of base disturbance during simulated SLAM loop transition.

In Fig. 1, all three square wave curves have an upper limit of 50 mm for the disturbance amplitude. Within the experimental period of 0 to 60 seconds, the duration of a single disturbance (high-level phase) corresponding to the three frequencies of 0.05 Hz, 0.2 Hz and 1.0 Hz is 10 seconds, 2.5 seconds and 0.5 seconds respectively. The number of step changes per unit time increases linearly with the frequency. The design of the three frequency gradients covers the complete disturbance frequency band from slow change at low frequency to fast change at high frequency. The uniform and fixed disturbance amplitude under each frequency condition is due to the active decoupling of the two disturbance attributes of the jump impact intensity and the jump frequency.

The design intent of fixing the disturbance amplitude and independently adjusting the frequency is to decouple the two disturbance attributes of jump impact intensity and jump frequency [24]. The amplitude of the real SLAM loop correction depends on the odometry cumulative drift, which increases with the path length and motion duration, so there is an inextricable correlation between the jump amplitude and the jump time [25]. The simulated injection method replaces the real drift with a fixed amplitude A_{jump}, forcing each jump to cause the impact intensity to the observation conditions to be equal, and the change of frequency f only affects the number of impacts per unit time. The decoupling of amplitude and frequency makes the difference in jitter amplitude observed at different frequency levels in subsequent experiments solely attributed to the combined effect of frequency change and denoising steps N, eliminating the interference of the jitter amplitude fluctuation as a confusing factor. After the disturbance injection, the instantaneous correction of the base pose estimation is transmitted to the target relative pose observation value through coordinate system transformation, thereby changing the input conditions of the Diffusion Policy, triggering the end effector's compensation response to the jump, and the jitter amplitude measurement channel is completely closed [26]-[27].

C. METHODS FOR EXTRACTING END-OF-TRAJECTORY JITTER AMPLITUDE

After the simulated SLAM loop jump is injected through the observation path, the compensation command generated by the Diffusion Policy drives the end effector of the robotic arm to superimpose high-frequency motion on the macroscopic task trajectory. This composite trajectory is recorded in real time by the onboard computing unit at a fixed sampling rate F_s. The sampling clock and the disturbance injection timing share the same trigger source to ensure that the end effector motion data and the jump event are strictly aligned on the time axis [28]. The original trajectory data collected in a single experiment constitutes a discrete time sequence $\{p_0, p_1, \ldots, p_M\}$, where $p_j = [x_j, y_j, z_j]^\top$ is the Cartesian coordinate of the end effector in the world coordinate system at the j-th sampling time, and $M = T \cdot F_s$ is the total number of sampling points.

The original trajectory sequence simultaneously carries the macroscopic task motion and the high-frequency jitter induced by the jump. The macroscopic motion is shaped by the preset path geometry and the low-frequency motion component generated by the Diffusion Policy, and its energy is concentrated in the low-frequency range [29]. The jitter component originates from the step response of the strategy to the SLAM jump and the transient adjustment of the servo loop, and the spectrum distribution shifts to a higher frequency band [30]. Taking advantage of the separation characteristics of the two in the frequency domain, a zero-phase low-pass digital filter is applied to the original sequence to extract the macroscopic motion trajectory. The filter adopts a finite impulse response structure, and the unit impulse response $h[k]$ is designed based on the cutoff frequency f_c using the window function method. The value of the cutoff frequency f_c must be higher than the highest frequency component of the macroscopic task motion and lower than the lowest characteristic frequency of the jump response. The former is determined by the rate of change of the path geometric curvature and the end linear velocity, while the latter is jointly determined by the equivalent bandwidth of the Diffusion Policy and the dynamic closed-loop of the servo loop. Through preliminary experiments and spectral analysis of the end trajectory under typical jump excitation, the midpoint of the frequency domain between the upper boundary of the main lobe of the macroscopic motion spectrum and the lower boundary of the first side lobe of the jump response spectrum is taken as the set value of f_c [31]. The macroscopic motion sequence $\{p_{\text{macro},j}\}$ is obtained by convolving the original sequence with the filter impulse response, while the jitter component sequence is obtained by subtracting the macroscopic sequence point by point from the original sequence:

$$p_{\text{jitter},j} = p_j - \sum_k h[k] \cdot p_{j-k} \tag{4}$$

This difference sequence completely preserves the high-frequency oscillation component excited at the end of the jump response, and its frequency composition quantitative characterization relies on amplitude-frequency characteristic analysis. The low-frequency main lobe in the original spectrum corresponds to the macroscopic motion contribution, while the high-frequency sidelobes and noise plateau reflect the jitter energy distribution. The low-pass filter applies stopband attenuation to the high-frequency components with a cutoff frequency of 150Hz f_c, thus preserving the macroscopic motion component within the passband. The amplitude-frequency characteristics before and after filtering are compared in Figure 2.

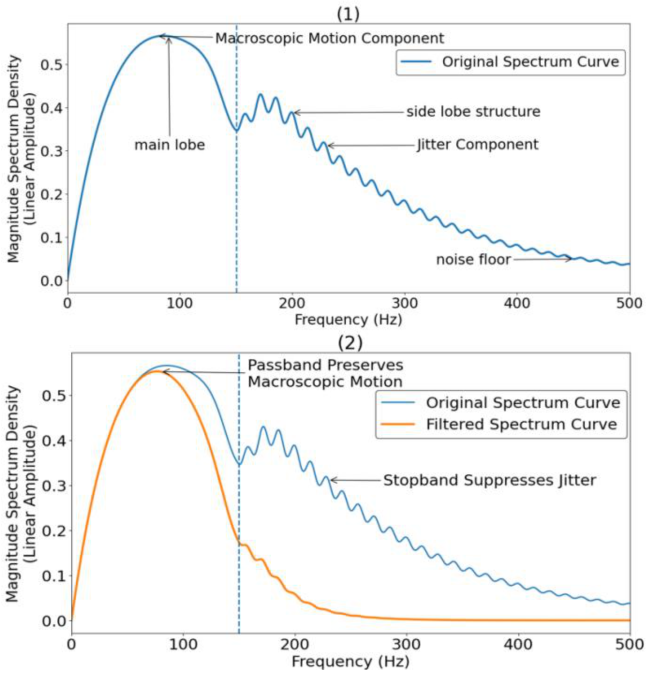

FIGURE 2. End trajectory amplitude spectrum structure and filtering effect. Fig. 2(1) Frequency band composition of the original trajectory amplitude spectrum. Fig. 2(2) Changes in amplitude spectrum before and after low-pass filtering.

In Fig. 2(1), the original spectrum exhibits a main lobe structure with a peak value of approximately 0.55 to the left of the 150Hz cutoff frequency, corresponding to the frequency concentration range of the macroscopic motion of the end effector; to the right of the cutoff frequency, a side lobe oscillation structure with gradually decreasing amplitude appears, accompanied by a noise floor that slowly decays in the high-frequency band. In Fig. 2(2), the filtered spectrum highly overlaps with part of the original curve in the passband, and the main lobe shape and peak amplitude are completely preserved. The amplitudes of the side lobe oscillations and noise floor in the stopband are significantly reduced. The filtered curve approaches zero after passing through a certain transition range above the cutoff frequency, thus enabling the macroscopic motion component and the high-frequency jitter component to be separated in the frequency domain.

The conversion from jitter component sequence to scalar jitter amplitude is accomplished by calculating the root mean square (RMS) value of the sequence. Actual trajectory acquisition uses discrete sampling points, but the sampling rate F_s is much higher than the highest frequency component of the jitter signal. The discrete RMS value is a precise approximation of the definition of continuous integral [32]-[33]. The jitter amplitude J is taken as the RMS value of the jitter component within a single trajectory duration T, and its continuous form is:

$$J = \sqrt{\frac{1}{T}\int_0^T \|p_{\text{jitter}}(t)\|_2^2 \, dt} \tag{5}$$

The motion path of the robotic arm and the disturbance amplitude of the base are kept fixed under different experimental conditions. In order to eliminate the inherent scale difference between paths and make the cross-condition comparison reflect only the joint effect of N and f, the reference jitter level J_{ref} is introduced to normalize J [34]. In order to intuitively reflect the relative suppression effect of the number of denoising steps at each jump frequency, J_{ref} is defined as the average jitter amplitude measured when N takes the lowest value of 4 at each jump frequency level. The normalized jitter amplitude $\hat{J} = J/J_{\text{ref}}$ reflects the degree of jitter change in the form of the ratio relative to the lowest bandwidth state at the same frequency, which is convenient for cross-frequency comparison. The $\hat{J}$ obtained by the above steps is the end jitter amplitude observation index of this experiment, which together with the corresponding number of denoising steps N and jump frequency f constitutes the complete data record of a single experiment.

D. STATISTICAL TEST SETTING OF THE INTERACTION EFFECT OF TWO INDEPENDENT VARIABLES

The influence of N and f on $\hat{J}$ needs to be determined through a standard statistical framework. If only the marginal effect of N at each level f or the marginal effect of f at each level N is examined, whether the observed jitter changes are due to the independent contributions of the two variables or the additional effect produced by their combined effect cannot be distinguished. Two-way ANOVA decomposes the total variation into main effect components and interaction effect components, providing a direct and rigorous test tool for answering the core question of this paper: whether N and f have an interaction effect on $\hat{J}$ [35]. The ANOVA model expresses $\hat{J}$ as a linear combination of the main effect of N, the main effect of f, the interaction effect of the two, and random error:

$$\hat{J}_{ijr} = \mu + \alpha_i + \beta_j + (\alpha\beta)_{ij} + \epsilon_{ijr} \tag{6}$$

In the formula, $\hat{J}_{ijr}$ is the jitter amplitude observed in the r-th repeated experiment when N is at level i and f is at level j; μ is the total mean; α_i is the main effect of N at level i; β_j is the main effect of f at level j; $(\alpha\beta)_{ij}$ is the interaction effect term of the two; ϵ_{ijr} is the random error, which is assumed to follow a normal distribution with zero mean and homogeneity of variance. The interaction effect term $(\alpha\beta)_{ij}$ captures the extent to which the influence of N on $\hat{J}$ varies with different levels of f. Whether this term is significantly non-zero directly determines the existence of the interaction.

Both N and f take multiple discrete levels, forming a full factorial experimental design. Each factor level combination is repeated an equal number of times to estimate the random error variance. The robotic arm's motion path, base disturbance amplitude, and the target object's relative pose remain constant in all experiments; these fixed conditions are not included in the ANOVA model, and their effects are absorbed into the overall mean μ. The time sequence of repeated experiments is completely randomized to eliminate the interference of potential time trends in the experimental process on the estimation of factor effects. Before the ANOVA, the model assumptions need to be tested. Residual normality is determined by the Shapiro-Wilk test, and homogeneity of variance is determined by the Levene test. If the hypothesis test fails, appropriate variable transformations are applied to $\hat{J}$ until the assumptions are satisfied. The significance test of the interaction effect is based on the F-statistic:

$$F_{\text{int}} = \frac{MS_{\text{int}}}{MS_{\text{error}}} \tag{7}$$

MS_{int} is the mean square of the interaction effect, and MS_{error} is the mean square of the error. Assuming the null hypothesis that the interaction effect term $(\alpha\beta)_{ij}$ is all zero and true, F_{int} follows an F-distribution with degrees of freedom $(df_{\text{int}}, df_{\text{error}})$. The significance threshold is set to $\alpha = 0.05$. If the p-value corresponding to F_{int} is less than this threshold, the null hypothesis is rejected, and the interaction effect is considered statistically significant. A significant interaction effect means that the direction and strength of N's influence on $\hat{J}$ depends on the level of f. In this case, the individual interpretation of the main effect is meaningless, and subsequent analysis should focus on comparing the simple effects of the two variables under different level combinations. An insignificant interaction effect indicates that the effects of the two variables on $\hat{J}$ are additive, and their respective main effects can be independently interpreted in a marginal sense. Regardless of whether the interaction effect is significant or not, the effect decomposition framework provided by ANOVA fully covers the logical link from data observation to statistical inference.

III. EXPERIMENTAL SETUP

A. HARDWARE AND SOFTWARE PLATFORM PARAMETERS

The experimental platform consists of three parts: an omnidirectional mobile chassis, a six-DOF collaborative robotic arm, and an onboard computing unit. The mobile chassis employs a Mecanum wheel drive structure, with a rated load no less than the mass of the robotic arm itself. Odometer data is transmitted between the chassis and the onboard computing unit via a Controller Area Network (CAN) bus. A six-dimensional force/torque sensor is installed at the end effector of the robotic arm. The joint controller operates in a closed-loop manner at a frequency of 1kHz and communicates with the onboard computing unit via Ethernet for Control Automation Technology (EtherCAT) in real-time, with control command latency not exceeding 1ms. The onboard computing unit is equipped with a 64-bit Advanced RISC Machine (ARM) architecture processor, running an Ubuntu 20.04 real-time kernel, and is responsible for the collaborative scheduling of LeRobot Diffusion Policy inference, SLAM module operation, and disturbance injection program.

The LeRobot framework uses the stable v1.0 version. The Diffusion Policy inference module is built on PyTorch 2.1, and the diffusion model backbone network is a temporal convolutional structure. The input dimension of the observation sequence covers the 6 joint angular positions and 6 joint angular velocities of the robotic arm, as well as the 6-DOF pose of the target object relative to the base coordinate system. The output dimension of the action sequence is the 6-DOF target pose of the end effector. The inference process is executed on the onboard Graphics Processing Unit (GPU), and the latency of a single inference does not exceed the control cycle at any denoising step level.

The SLAM jump injection procedure runs as an independent Robot Operating System 2 (ROS2) node. It subscribes to the original base pose topics published by the SLAM module, superimposes a base step perturbation sequence with fixed amplitude and adjustable time intervals onto the SLAM observation path, and then republishes it. The rotation component of the perturbation transformation matrix maintains an identity matrix to eliminate additional contributions from rotational degrees of freedom, while the translation component amplitude is fixed to a constant value to ensure equal impact intensity for each jump. The Diffusion Policy observation module subscribes to the injected pose topics. The injection node and the data acquisition node share the same ROS2 clock source. The jump trigger time and the end-point trajectory sampling timestamp are strictly aligned on a unified time axis, with a time synchronization error not exceeding 2ms, satisfying the requirement that the time interval between adjacent sampling points at a 500Hz sampling rate be within 10%.

B. VARIABLE LEVELS AND DATA ACQUISITION SETTINGS

The denoising step count N is set to four discrete levels in the experiment: $N \in \{4, 16, 32, 64\}$. $N = 4$ corresponds to the widest bandwidth configuration of the policy, making the action generation path most sensitive to changes in observations; $N = 64$ corresponds to the narrowest bandwidth configuration, providing the strongest temporal smoothness of the action sequence but exhibiting the largest phase lag in response to external abrupt changes; $N = 16$ and $N = 32$ serve as intermediate levels, covering the complete transition range from wide to narrow bandwidth. The simulated SLAM loop transition frequency f is set to three discrete levels: $f \in \{0.05, 0.2, 1.0\}$Hz, corresponding to adjacent same-direction transition time intervals Δt of 20 seconds, 5 seconds, and 1 second, respectively. $f = 0.05$Hz represents a low-frequency sparse perturbation scenario, allowing ample time for the system to adjust between adjacent transitions; $f = 1.0$Hz represents a high-frequency dense perturbation scenario, with the transition time interval on the same order of magnitude as the policy adjustment time constant; $f = 0.2$Hz serves as an intermediate level, covering the complete frequency gradient from sparse to dense. The disturbance amplitude is fixed at $A_{\text{jump}} = 50$mm, and the disturbance direction is cyclically selected within the horizontal plane according to a preset angle set.

A total of 12 experimental conditions are formed by 4×3 full factorial combinations of N and f. Five independent repeated experiments are performed under each condition. Between repeated experiments, the robotic arm's motion path, the target's initial pose, and the base's docking position are reset to eliminate the influence of residual states between experiments. The trajectory acquisition time for each experiment is 60 seconds. The end effector's Cartesian coordinates are recorded in real time at a sampling rate of 500Hz. The raw trajectory data acquired in a single experiment consists of 30,000 sampling points. The low-pass filter cutoff frequency is set to 150Hz to separate macroscopic motion components from high-frequency jitter components.

IV. RESULTS

A. DISTRIBUTION PATTERN OF JITTER AMPLITUDE IN PARAMETER SPACE

To fully reveal the joint effect pattern of denoising steps and SLAM loop transition frequency in parameter space, the experiment collects the normalized jitter amplitude of the end effector under 12 parameter combinations consisting of 4 denoising step levels ($N = 4$, 16, 32, 64) and 3 transition frequency levels ($f = 0.05$, 0.2, 1.0Hz). The mean values of each group are filled into a two-dimensional matrix with denoising steps as the vertical axis and transition frequency as the horizontal axis. The spatial distribution pattern of jitter intensity is visualized by chromaticity mapping to determine whether there is a nonlinear coupling trend between the two variables, as shown in Figure 3.

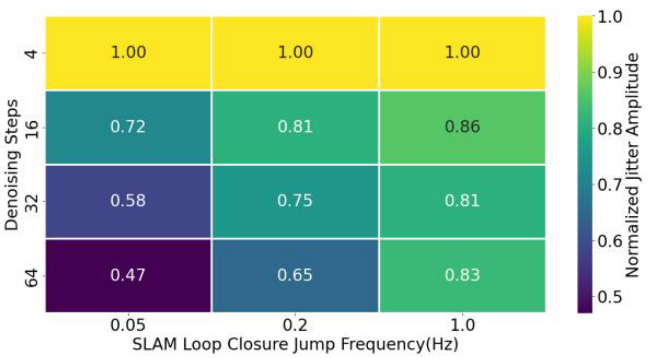

FIGURE 3. Heatmap distribution of normalized jitter amplitude on the denoising step count-jump frequency parameter plane.

Fig. 3 reveals a significant asymmetric gradient structure, indicating the conditional dependence between the two variables. At $f = 0.05$Hz, the normalized jitter amplitude monotonically decreases from 1.00 to 0.47 as N increases from 4 to 64, a decrease of 53 percentage points, indicating that narrowing the strategy bandwidth in low-frequency disturbance environments has a sustained suppressive effect on high-frequency oscillations. When f rises to 1.0Hz, the jitter amplitude only decreases from 1.00 to 0.83 under the same N increment, with the net attenuation shrinking to 17 percentage points. Furthermore, the jitter difference between $N = 32$ and $N = 64$ is only 0.02, indicating that the downward trend is approaching saturation. This divergence stems from the fact that the temporal density of the disturbance signal under high-frequency jump conditions exceeds the effective response range of the strategy bandwidth corresponding to a large number of denoising steps. The action generation path, due to insufficient bandwidth, cannot compensate for dense impacts in time, resulting in low-frequency overcompensation accumulation, which drastically reduces the marginal benefit of jitter suppression.

B. VISUALIZATION OF THE INTERACTION EFFECT BETWEEN DENOISING STEPS AND JUMP FREQUENCY

The global distribution pattern on the parameter plane only reflects the spatial location of the jitter amplitude under the combined effect of the two variables, and cannot separate and compare the marginal effect strength of a single independent variable at different levels of the other independent variable. To clarify the independent influence of the number of denoising steps on the jitter amplitude of the end effector under different jump frequencies, the experiment fixes the jump frequencies at three levels: 0.05 Hz, 0.20 Hz, and 1.00 Hz. Under each frequency constraint, the evolution trajectory of the normalized jitter amplitude is independently observed as the number of denoising steps increases from 4 to 64. This operation provides a direct test for the existence of interaction effects by separating the marginal effects of a single independent variable. The corresponding results are shown in Figure 4.

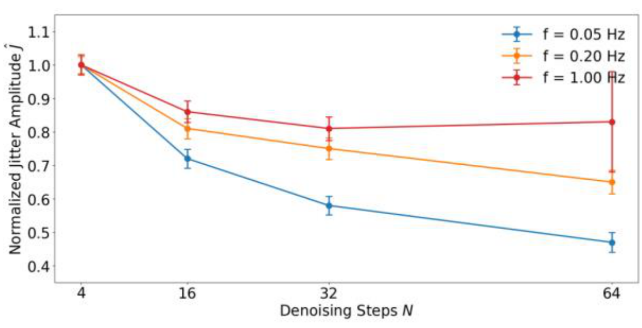

FIGURE 4. Simple effect curves of the number of denoising steps at different transition frequency levels on the normalized jitter amplitude of the end effector.

Fig. 4 shows the independent impact of the number of denoising steps on the normalized jitter amplitude when the jump frequency is fixed at 0.05Hz, 0.20Hz, and 1.00Hz, respectively. At 0.05Hz, the line slopes steeply downwards with increasing denoising steps, exhibiting the largest absolute slope among the three. This reflects that low-frequency sparse disturbances provide ample response recovery time for the system, allowing the low-pass filtering effect of the denoising steps to fully attenuate oscillation energy after each impact, resulting in a continuous accumulation of suppression. At 0.20Hz, the line slope narrows, and the decline is significantly weakened, indicating that the strategy adjustment margin is partially squeezed after the disturbance interval is shortened. At 1.00Hz, the line flattens out at the high end of the denoising step count, and further increasing the denoising step count contributes almost no additional jitter attenuation. This reveals that high-frequency dense disturbances cause the narrow-bandwidth action path to encounter new impacts before the previous response converges, and the low-frequency overcompensation accumulation effect dominates the evolution direction of jitter energy. The systematic attenuation of the slope of the three broken lines as the fixed frequency increases confirms the negative modulation of the denoising step suppression strength by the jump frequency, that is, the increase in frequency weakens the smoothing gain that the denoising step should bring, and the two constitute an antagonistic interaction.

C. FREQUENCY DOMAIN RECONSTRUCTION AND MECHANISM ELUCIDATION OF JITTER ENERGY

The aforementioned simple effect analysis reveals an antagonistic interaction pattern where the suppression strength of the jitter amplitude by the number of denoising steps systematically decreases with increasing jump frequency. This pattern has been confirmed at the parameter level, but its formation mechanism at the frequency domain energy level remains to be elucidated. Therefore, the Welch method is used to estimate the one-sided power spectral density of the complete jitter time-domain signal acquired under all parameter combinations. Power spectral density curves corresponding to four different denoising steps are presented in a logarithmic coordinate system under two jump frequency conditions: $f = 0.05$Hz and $f = 1.0$Hz. Figure 5 compares the systematic changes in the strategy bandwidth adjustment effect with perturbation frequency conditions from the perspective of frequency domain energy distribution.

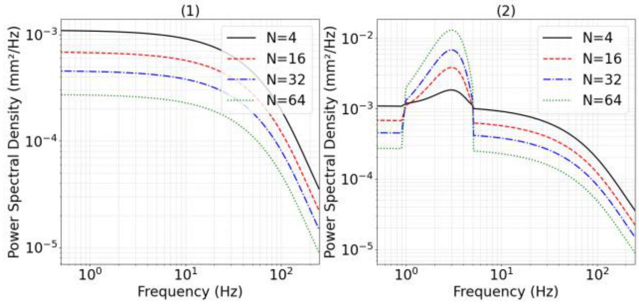

FIGURE 5. Comparison of power spectral density of jitter signal corresponding to different denoising steps under low-frequency and high-frequency disturbance backgrounds. Fig. 5(1) Power spectral density curves of each denoising step under the condition of $f = 0.05$Hz frequency jump. Fig. 5(2) Power spectral density curves of each denoising step under the condition of $f = 1.0$Hz frequency jump.

Fig. 5(1) and 5(2) show diametrically opposed frequency domain energy evolution patterns under two different frequency jump backgrounds. In Figure 5(1), under the condition of $f = 0.05$Hz, when N increases from 4 to 64, the power spectral density curve of the entire frequency band shifts downward as a whole. The power spectral density of the low frequency band corresponding to $N = 4$ is on the order of 10^{-3} mm^2/Hz, and the curve of $N = 64$ drops by about half an order of magnitude at the same frequency. This uniform wideband attenuation is due to the fact that the system has sufficient time to complete transient adjustment between two adjacent jumps under low-frequency sparse disturbance. The low-pass effect of large noise reduction steps has fully dissipated the oscillation energy before the disturbance reappears, and the suppression effect of bandwidth narrowing can be linearly accumulated in the entire frequency band. In Figure 5(2), under the condition of $f = 1.0$Hz, the curves of $N = 64$ and $N = 32$ show obvious energy bulges in the low-frequency range of 1 to 5Hz, with peak power spectral density on the order of 10^{-2} mm^2/Hz, which is about an order of magnitude higher than that of $N = 4$ in this frequency band. However, in the high-frequency range above 10Hz, the curve of large N is lower than that of small N. The root cause of this low-frequency energy overtaking phenomenon is that the high-frequency dense jump shortens the time interval between adjacent disturbance impacts to within the strategy adjustment time constant. The narrow bandwidth action generation path corresponding to the large number of denoising steps cannot complete the compensation convergence before the next impact arrives. The residual compensation amount and the new impact response are superimposed and accumulated in the low-frequency range, forming an overcompensated accumulation peak. Although the high-frequency oscillation is suppressed, the nonlinear accumulation of low-frequency energy dominates the overall trend of the root mean square jitter amplitude. The comparison in Figure 5 shows that the effect of the number of denoising steps on the jitter energy adjustment has a strong conditional dependence in the frequency domain. The relative relationship between the disturbance frequency and the strategy bandwidth determines whether energy suppression or energy accumulation becomes the dominant mechanism.

D. STATISTICAL INFERENCE AND PARAMETER BOUNDARY CALIBRATION OF INTERACTION EFFECTS

Simple effect analysis confirms the existence and form of the interaction effect, while frequency domain analysis reveals its energy-level formation mechanism. Together, they complete a mechanistic explanation of the combined effect of denoising steps and frequency jumps. Based on this, the experimental data needs to be transformed into quantitative parameter constraints for engineering deployment to clarify the feasible selection range of denoising steps in different frequency jump environments. Therefore, based on the measured three frequency levels and four denoising step levels, spline interpolation is used to expand the parameter plane into a dense 7×7 grid. The distribution pattern of the normalized jitter amplitude in the continuous parameter space is presented in the form of filled contour lines. The node values in the high-frequency, high-denoising-step region are extrapolated estimates based on the measured data, reflecting the predicted behavior of this parameter interval under more dense perturbation conditions. A safety boundary is drawn with a normalized jitter amplitude of 1.05 as the acceptable threshold for engineering, dividing the parameter plane into recommended and unrecommended working areas, as shown in Fig. 6.

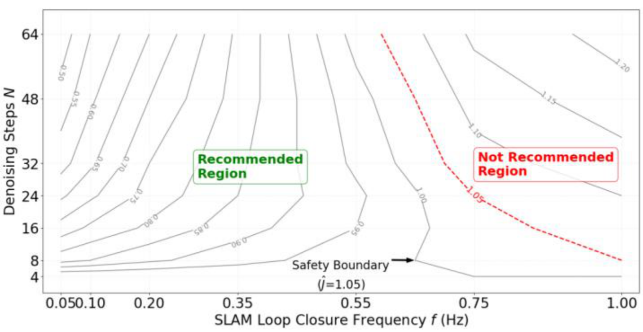

FIGURE 6. Contour lines of normalized jitter amplitude on the plane of denoising steps and SLAM loopback frequency parameters, and engineering safety boundary.

The contour lines and the spatial orientation of the safety boundary in Figure 6 together reveal the nonlinear coupling structure of the two variables constraining the smoothness of the terminal trajectory. In the $f \leq 0.35$Hz range, the normalized jitter amplitude contour lines are generally biased to the left of the parameter plane, and the jitter amplitude corresponding to $N = 64$ is as low as 0.47. The safety boundary does not constrain the upper limit of the number of denoising steps in this frequency band, and it is recommended that the working area cover the entire N level. This pattern is due to the continued effectiveness of the suppression effect of the narrowing strategy bandwidth under low-frequency sparse perturbation. The contour line spacing in the left region of the parameter plane is uniform, and the jitter amplitude decreases approximately monotonically with N and approaches the safety threshold. When f exceeds approximately 0.55 Hz, the contour lines bend significantly on the right side of the parameter plane; the spacing narrows sharply; and the lines tilt towards the higher N direction. The safety boundary, represented by the red dashed line, starts at approximately $f = 0.60$ Hz and $N = 8$, and rapidly contracts towards the lower N direction as the frequency increases. By $f = 1.0$ Hz, the maximum allowable denoising steps corresponding to the safety boundary have decreased to around $N = 8$. This contraction reflects the geometric projection in the parameter space of the mechanism that causes low-frequency overcompensation accumulation due to a large number of denoising steps under high-frequency dense transitions. After the ratio of the perturbation frequency to the policy adjustment time constant exceeds the critical point, increasing N no longer improves but worsens the trajectory smoothness. The safety boundary thus forms a constraint curve that monotonically tightens with frequency. The joint analysis of the contour surface and the safety boundary provides a quantitative parameter boundary with engineering operability for the selection of the number of denoising steps in LeRobot Diffusion Policy under different SLAM loopback frequency scenarios.

E. REPEATED EXPERIMENTAL VERIFICATION OF SYSTEM ROBUSTNESS

Mean-level parameter effect analysis is insufficient to assess the operational reliability of the system in actual deployment scenarios. The dispersion between jitter observations in a single experiment and multiple repetitions also constitutes a key criterion for engineering applicability. Therefore, the normalized jitter amplitude raw observations from five independent repetitions under 12 sets of parameters are presented in the form of box plots, with semi-transparent scatter plots superimposed to indicate all 60 independent measurements. Three jump frequencies are distinguished by color within the same coordinate system. The stability of the system operation under each parameter combination is simultaneously evaluated from two dimensions: the central tendency and the dispersion of the data distribution, as shown in Fig. 7.

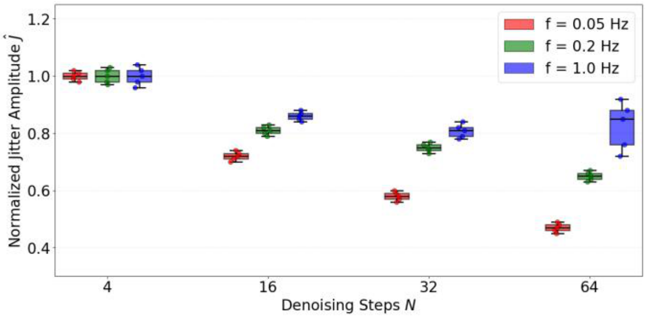

FIGURE 7. Box plot distribution characteristics of normalized jitter amplitude in 5 repeated experiments under various parameter combinations.

Fig. 7 shows a significant structural differentiation in the dispersion of normalized jitter amplitude in repeated experiments under different parameter combinations. Under low-frequency jump conditions, repeated observations at each denoising step level are highly concentrated, with interquartile ranges mostly not exceeding 0.04, indicating strong determinism in the system response. Under high-frequency jump conditions, when the number of denoising steps increases to 64, the interquartile range expands sharply to approximately 0.10, and the fluctuation amplitude of jitter amplitude between single experiments exceeds the mean difference between different denoising step levels by an order of magnitude. This abrupt change in dispersion reveals that the dynamic adjustment process of the large denoising step strategy in a high-frequency dense perturbation environment is highly sensitive to initial conditions and perturbation timing, and the randomness of the superposition effect of adjacent impacts is amplified in a narrow bandwidth path. The systematic change in the dispersion of repeated experiments with parameter combinations indicates that evaluating the quality of parameters solely based on the mean level under high-frequency perturbation conditions can mask the risk of the system entering an unreliable operating range, and robustness constraints and mean constraints have equal importance in the selection of engineering parameters.

V. CONCLUSION

The core finding of this paper is that the effect of the number of denoising steps on the amplitude of trajectory jitter in the end effector is not a monotonic relationship in a fixed direction, but rather exhibits a conditionally dependent reversal with the SLAM loop transition frequency level. This conclusion breaks the intuitive assumption that "a higher number of denoising steps necessarily leads to a smoother trajectory," revealing an implicit frequency matching constraint between the strategy bandwidth and the external disturbance frequency. From the perspective of frequency domain energy distribution, the physical root of this constraint lies in the fact that when the transition frequency exceeds the critical value corresponding to the strategy adjustment time constant, the low-frequency over-compensation accumulation effect of the narrow-bandwidth action generation path becomes the dominant mechanism. Its negative contribution to the root mean square jitter amplitude outweighs the benefits brought by high-frequency oscillation suppression, making a large number of denoising steps both worsen the jitter mean and significantly amplify the performance dispersion between repeated experiments in a high-frequency disturbance environment. The engineering significance of this finding is that the selection of the number of denoising steps cannot be determined independently of the loop transition frequency characteristics of the deployment environment; the joint configuration of the two must refer to the safety boundary constraints under frequency conditions. The limitations of this paper are reflected in two aspects: the perturbation amplitude is fixed as a single constant value in the experiment, while the odometer drift dynamically changes with the driving path in real-world scenarios, and the impact of amplitude fluctuations on the interaction effect boundary has not been included in the analysis; the experimental conclusions are based on specific robotic arm configurations and chassis kinematic parameters, and the generalization applicability of the parameter boundary to different hardware platforms needs to be systematically verified. Future research directions lie in introducing variable amplitude perturbation conditions to extend the two-dimensional parameter boundary of this paper into a three-dimensional constrained surface composed of amplitude, frequency, and denoising steps, and on this basis, exploring an adaptive adjustment mechanism for the number of denoising steps based on online jump frequency estimation to support the robust deployment of LeRobot Diffusion Policy in complex unstructured environments.

REFERENCES

[1] W. Hao, P. Wang, C. Ni, W. Huangfu, Z. Liu, and K. Qi, "Loop closure detection based on image feature matching and motion trajectory similarity for mobile robot," Applied Intelligence, vol. 55, no. 7, pp. 447–455, 2025, doi: 10.1007/s10489-024-05874-4.

[2] C. Chi, Z. Xu, S. Feng, E. Cousineau, Y. Du, B. Burchfiel, et al., "Diffusion policy: Visuomotor policy learning via action diffusion," The International Journal of Robotics Research, vol. 44, no. 10–11, pp. 1684–1704, 2025, doi: 10.1177/02783649241273668.

[3] C. Yu, Z. Chao, H. Xie, Y. Hua, and W. Wu, "An Enhanced Multi-Sensor Simultaneous Localization and Mapping (SLAM) Framework with Coarse-to-Fine Loop Closure Detection Based on a Tightly Coupled Error State Iterative Kalman Filter," Robotics, vol. 13, no. 1, pp. 2–11, 2023, doi: 10.3390/robotics13010002.

[4] Y. Cai, Y. Ou, and T. Qin, "Improving SLAM techniques with integrated multi-sensor fusion for 3D reconstruction," Sensors, vol. 24, no. 7, pp. 2033–2039, 2024, doi: 10.3390/s24072033.

[5] S. Arshad and G. W. Kim, "Role of deep learning in loop closure detection for visual and lidar slam: A survey," Sensors, vol. 21, no. 4, pp. 1243–1250, 2021, doi: 10.3390/s21041243.

[6] C. E. Denniston, Y. Chang, A. Reinke, K. Ebadi, G. S. Sukhatme, and L. Carlone, "Loop closure prioritization for efficient and scalable multi-robot SLAM," IEEE Robotics and Automation Letters, vol. 7, no. 4, pp. 9651–9658, 2022, doi: 10.1109/LRA.2022.3191156.

[7] J. Carvalho, A. T. Le, P. Kicki, D. Koert, and J. Peters, "Motion planning diffusion: Learning and adapting robot motion planning with diffusion models," IEEE Transactions on Robotics, vol. 41, no. 1, pp. 4881–4901, 2025, doi: 10.1109/TRO.2025.3593109.

[8] H. Qiu, Z. Chen, Z. Wang, Y. He, M. Xia, and Z. Liu, "FreeTraj: Tuning-Free Trajectory Control via Noise Guided Video Diffusion," International

Journal of Computer Vision, vol. 134, no. 4, pp. 165–172, 2026, doi: 10.1007/s11263-026-02732-3.

[9] X. Shi, Y. Hu, and J. Jin, "FRMD: fast robot motion diffusion via trajectory-level consistency distillation," Frontiers in Robotics and AI, vol. 13, no. 1, pp. 1751688–1751694, 2026, doi: 10.3389/frobt.2026.1751688.

[10] H. Ding, N. Jaquier, J. Peters, and L. Rozo, "Fast and robust visuomotor riemannian flow matching policy," IEEE Transactions on robotics, vol. 41, no. 1, pp. 5327–5343, 2025, doi: 10.1109/TRO.2025.3601293.

[11] J. Zhu, H. Li, and T. Zhang, "Camera, LiDAR, and IMU based multi-sensor fusion SLAM: A survey," Tsinghua Science and Technology, vol. 29, no. 2, pp. 415–429, 2023.

[12] T. Xu, M. Chen, and J. Liu, "TKO-SLAM: Visual SLAM algorithm based on time-delay feature regression and keyframe pose optimization," Journal of Field Robotics, vol. 41, no. 6, pp. 1960–1983, 2024, doi: 10.1002/rob.22357.

[13] Y. Lian, X. Xiao, J. Zhang, L. Jin, J. Yu, and Z. Sun, "Neural dynamics for cooperative motion control of omnidirectional mobile manipulators in the presence of noises: A distributed approach," IEEE/CAA Journal of Automatica Sinica, vol. 11, no. 7, pp. 1605–1620, 2024, doi: 10.1109/JAS.2024.124425.

[14] R. Wolf, Y. Shi, S. Liu, and R. Rayyes, "Diffusion models for robotic manipulation: A survey," Frontiers in Robotics and AI, vol. 12, no. 1, pp. 1606247–1606254, 2025, doi: 10.3389/frobt.2025.1606247.

[15] C. Pan, Z. Yi, G. Shi, and G. Qu, "Model-based diffusion for trajectory optimization," Advances in Neural Information Processing Systems, vol. 37, no. 1, pp. 57914–57943, 2024, doi: 10.52202/079017-1846.

[16] S. Zheng, J. Wang, C. Rizos, W. Ding, and A. EI-Mowafy, "Simultaneous localization and mapping (slam) for autonomous driving: Concept and analysis," Remote Sensing, vol. 15, no. 4, pp. 1156–1162, 2023, doi: 10.3390/rs15041156.

[17] X. Jiang, L. Zhu, J. Liu, and A. Song, "A SLAM-based 6DoF controller with smooth auto-calibration for virtual reality," The Visual Computer, vol. 39, no. 9, pp. 3873–3886, 2023, doi: 10.1007/s00371-022-02530-1.

[18] M. Iqbal, R. A. M. Qureshi, and G. Abbas, "SIMULATING THE TIME-VARYING PARAMETERS OF ROBOTS IN PERFORMING THE COMPLEX SEQUENTIAL TASKS," Pakistan Journal of Scientific Research, vol. 4, no. 1, pp. 93–104, 2024, doi: 10.57041/vol4iss1pp93-104.

[19] C. Li, Z. Liu, L. Li, Z. Ji, C. Li, J. Liang, et al., "Improved PPO Optimization for Robotic Arm Grasping Trajectory Planning and Real-Robot Migration," Sensors, vol. 25, no. 17, pp. 5253–5260, 2025, doi: 10.3390/s25175253.

[20] Y. Guo, Y. Hu, J. Zhang, et al., "Prediction with action: Visual policy learning via joint denoising process," Advances in Neural Information Processing Systems, vol. 37, no. 1, pp. 112386–112410, 2024, doi: 10.52202/079017-3570.

[21] Y. Wang, Y. Tian, J. Chen, K. Xu, and X. Ding, "A survey of visual SLAM in dynamic environment: The evolution from geometric to semantic approaches," IEEE Transactions on Instrumentation and Measurement, vol. 73, no. 1, pp. 1–21, 2024, doi: 10.1109/TIM.2024.3420374.

[22] K. Kawaharazuka, J. Oh, J. Yamada, et al., "Vision-language-action models for robotics: A review towards real-world applications," IEEE Access, vol. 13, no. 1, pp. 162467–162504, 2025, doi: 10.1109/ACCESS.2025.3609980.

[23] I. Jebellat and I. Sharf, "Motion planners for path or waypoint following and end-effector sway damping with dynamic programming," IEEE Transactions on Automation Science and Engineering, vol. 22, no. 1, pp. 8439–8452, 2024, doi: 10.1109/TASE.2024.3486040.

[24] M. Wang, S. Lyu, Q. Liu, Z. Yang, K. Guo, and X. Yu, "Precise end-effector control for an aerial manipulator under composite disturbances: Theory and experiments," IEEE Transactions on Automation Science and Engineering, vol. 22, no. 1, pp. 4006–4021, 2024, doi: 10.1109/TASE.2024.3406754.

[25] H. Pan, D. Liu, J. Ren, T. Huang, and H. Yang, "LiDAR-IMU tightly-coupled SLAM method based on IEKF and loop closure detection," IEEE Journal of Selected Topics in Applied Earth Observations and Remote Sensing, vol. 17, no. 1, pp. 6986–7001, 2024, doi: 10.1109/JSTARS.2024.3357536.

[26] D. C. Hoang, J. A. Stork, and T. Stoyanov, "Voting and attention-based pose relation learning for object pose estimation from 3D point clouds," IEEE Robotics and Automation Letters, vol. 7, no. 4, pp. 8980–8987, 2022, doi: 10.1109/LRA.2022.3189158.

[27] R. Kranthi and Vasundhara, "A robust adaptive filter for diffusion strategy-based distributed active noise control," IETE Journal of Research, vol. 70, no. 5, pp. 5066–5080, 2024, doi: 10.1080/03772063.2023.2222099.

[28] M. B. Kadri, S. A. Khatri, and S. Yousuf, "Trajectory Tracking Control of a Planar Robotic Arm Using Inverse Dynamics and Fuzzy Gain Scheduling: Simulation and Experimental Validation," IEEE Access, vol. 13, no. 1, pp. 186736–186759, 2025, doi: 10.1109/ACCESS.2025.3626418.

[29] Q. Zhang, S. Feng, S. Chen, W. Teng, and Y. Qi, "Motion In-Betweening via Frequency-Domain Diffusion Model," Computers, Materials, & Continua, vol. 86, no. 1, pp. 1–9, 2026, doi: 10.32604/cmc.2025.068247.

[30] S. Sakhrieh, A. Singh, J. Mounsef, B. Arain, and N. Maalouf, "VIO-GO: optimizing event-based SLAM parameters for robust performance in high dynamic range scenarios," Frontiers in Robotics and AI, vol. 12, no. 1, pp. 1541017–1541024, 2025, doi: 10.3389/frobt.2025.1541017.

[31] F. Bjelonic, A. Sachtler, A. Albu-Schäffer, and C. D. Santina, "Experimental closed-loop excitation of nonlinear normal modes on an elastic industrial robot," IEEE Robotics and Automation Letters, vol. 7, no. 2, pp. 1689–1696, 2022, doi: 10.1109/LRA.2022.3141156.

[32] F. A. C. Alegria, "Contribution of jitter and phase noise to the precision of sinusoidal amplitude estimation using coherent sampling," Sci, vol. 7, no. 2, pp. 44–53, 2025, doi: 10.3390/sci7020044.

[33] B. Wang, Y. Peng, H. Jin, and J. Zhao, "Reciprocal Neural State–Disturbance Observer for Model-Free Trajectory Tracking of Robotic Manipulators," Mathematics, vol. 14, no. 6, pp. 983–991, 2026, doi: 10.3390/math14060983.

[34] S. Yin, Z. Shi, Y. Liu, G. Xue, and H. You, "Adaptive Non-Singular terminal sliding mode trajectory tracking control of robotic manipulators based on disturbance observer under unknown Time-Varying disturbance," Processes, vol. 13, no. 1, pp. 266–271, 2025, doi: 10.3390/pr13010266.

[35] S. Bonnini, M. Borghesi, G. Piscopo, and M. Giacalone, "A Non-Parametric Test for a Two-Way Analysis of Variance," Mathematics, vol. 13, no. 7, pp. 1131–1138, 2025, doi: 10.3390/math13071131.